24th Symposium on Naval Hydrodynamics
Fukuoka, JAPAN, 8-13 July 2002

An experimental and computational study of three-dimensional unsteady flow features found behind a truncated cylinder

R.J. Pattenden, S.R. Turnock and N.W. Bressloff
(University of Southampton, U.K.)

Abstract

The numerical prediction of three-dimensional turbulent separation regions and the resulting unsteady vortical flow patterns within these regions is still poor. This paper presents detailed experimental data for steady onset flow around a truncated cylinder of height/diameter ratio of 1.0, mounted on a ground plane. Measurements of unsteady surface pressures, total forces and particle image velocimetry describe the flow at a Reynolds number of 2.9×10^5. The performance of Large Eddy Simulation (LES) and Unsteady Reynolds-Averaged Navier Stokes (URANS) methods are compared for this case. It is seen that on ana identical grid, the LES simulations predict the separation region more accurately than the URANS model and at 75% of the computational cost.

C_D	Drag coefficient
C_p	Pressure coefficient
d	Diameter of cylinder (m)
δ	Thickness of boundary layer (m)
f	Frequency (Hz)
h	Height of cylinder (m)
p	Pressure (N/m^2)
p_∞	Tunnel static pressure (N/m^2)
ϕ	Angle from fwd stagnation point $(degrees)$
Re	Reynolds number based on diameter
Str	Strouhal number
U, V, W	Mean velocities along x, y and z (m/s)
U_∞	Free stream velocity (m/s)
x, y, z	Coordinate axes in streamwise, lateral (m) and vertical directions respectively, with origin at bottom centre of the cylinder

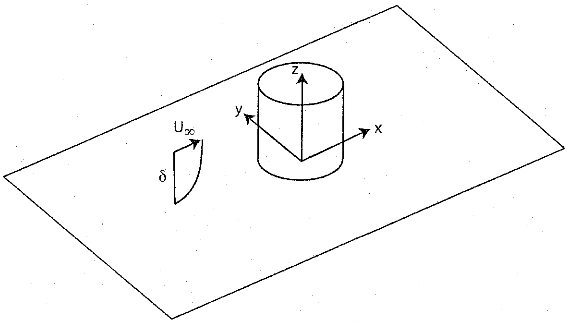

Figure 1: Diagram showing axes and flow direction

1 Introduction

The use of computational fluid dynamics (CFD) in hydrodynamics is becoming more widespread for design studies. However there are still some flow situations where the performance of these codes can be poor. One of these situations is the prediction of three-dimensional turbulent separation regions and the resulting unsteady vortical flow patterns within these regions. Such flows can occur at the sterns of ships such as tankers, around offshore structures, ship superstructures or submarine bridge fins. The ability to model such flows accurately is important if CFD is to be used as a reliable tool for the prediction of unsteady forces and resultant vibrations.

This paper presents the results of an experimental study into the flow around a truncated cylinder mounted on a ground plane together with some initial CFD results on the same geometry. The aim of this work is to build up an experimental database which will then be used for the validation of CFD simulations. The case was chosen as it contains many of the characteristics of typical marine flows. The geometry chosen for this study is that of a truncated cylinder, of $h/d = 1$, mounted on a ground plane which is a relative simple geometry to model both computationally and experimentally. This is representative of a complex three-dimensional separated flow, with a highly turbulent recirculation region and some pronounced unsteady vortical structures being formed. Capturing the physics of the unsteady vortices and vortex breakdown as well as the unsteady turbulent separation present considerable challenges both to experimental work and numerical simulations.

This paper will first present the set of experimental data which was used for comparison with the numerical results. Details will then be presented of the various computational simulations carried out, including unsteady RANS and some preliminary LES calculations.

2 Background

The flow around cylinders has been extensively studied throughout the history of fluid dynamics research, due to it's combination of geometrical simplicity and complex flow features. The majority of this work however has concentrated on two-dimensional flow or three-dimensional flow on an infinitely long cylinder. This situation is the one which gives rise to the famous Von Karman vortex shedding pattern. The case of a truncated cylinder of low aspect ratio, mounted on a wall, however gives a very different flow pattern.

The effects of varying the aspect ratio of circular cylinders has been studied by Farivar (1981) who identified three layers of vortex shedding with shedding frequency increasing toward the base: this lower region having a Strouhal number of similar value to the two-dimensional case. Ayoub and Karemcheti (1982) also showed that a shedding regime exists in the tip region that is distinct to that over the rest of the length. More recently the effects of the free end on the near wake were investigated by Park and Lee (2000), who discussed the effect of the counter rotating vortices formed at the free end. They attributed the three dimensionality to the downwash caused by these vortices.

Many investigations (see for example Baker (1979) and Visbal (1991)) have been carried out into the nature of the so-called "horseshoe" vortex which occurs at the juncture of a protrusion on a surface, such as where a cylinder is mounted on a ground plane. This vortex is formed when the flow on the surface upstream of the cylinder separates due to the adverse pressure gradient. The vortex formed here then trails downstream around the cylinder. Measurements of the shear stress on the ground under the vortex were made by Sumer et al. (1997).

Experiments on low aspect ratio cylinders are less common. Okamoto and Yagita (1973), took surface pressure measurements on cylinders with aspect ratios varying from 1 to 12.5 to find the drag coefficients as a function of aspect ratio. The drag coefficient was found to decrease with decreasing aspect ratio. They also noted that periodic vortex shedding does not exist at $h/d \leq 6$ as the effects of the free end reach the base. Okamoto (1982) studied the flow over a cylinder of aspect ratio 1 and a hemisphere capped cylinder. It was found that the vortices shed from the cylinder were symmetric arch vortices which shed at a Strouhal number of 0.225. Measurements were made of surface pressures and turbulence in the wake. Okamoto and Sunabashiri (1992) studied the changes in vortex formation with varying aspect ratio. It was found that the vortex shedding pattern changed from symmetric "arch" to antisymmetric "Karman" vortices at $h/d = 4$.

Sin and So (1987) measured local unsteady forces on a part of the span for different aspect ratios down to 1. They found that there was no suppressed two-dimensional region for the low aspect ratio cylinders and the strength of the force fluctuations was very small at $h/d < 1.5$. The band width of the shedding frequency was also much greater, due to the interference of the tip flow on the transverse shedding. This agrees with Luo et al. (1996) who only detected vortex shedding at $h/d = 8$, and Kawamura et al. (1984) who performed flow visualisation and found no von Karman shedding below $h/d = 5 \sim 6$, depending on the thickness of the oncoming boundary layer.

The mean flow around a truncated cylinder of aspect ratio 1 can be seen to be composed of three distinct flow features; that is the flow over the free end, the arch vortex and the horseshoe vortex, which interact strongly with each other, generating a fully three-dimensional flow. At a high Reynolds number, when the flow is fully turbulent there will be considerable unsteadiness in the wake region. Certain characteristics of this flow are similar to those found around the stern of full-sectioned ships such as tankers, in particular the tip vortices and trailing longitudinal vortex are similar to the bilge vortex. Likewise the separation region has some similarities to that at the stern of a ship. This type of flow presents a considerable challenge to CFD codes due to the separation on the curved surface, the anisotropic nature of the turbulence and the large scale turbulent fluctuations. The case of a truncated cylinder is therefore a useful one for the validation of codes destined for use in marine CFD.

While many calculations have been, and still are being, performed on complex geometries, both in industry and in academia, the majority use Reynolds-averaged Navier-Stokes (RANS) solvers with simple statistical turbulence models. Such models would have difficulty capturing all the complex flow features which occur behind bluff bodies. A steady-state RANS solver will only resolve the mean flow pattern with all the turbulent scales being modelled. Even an unsteady RANS (URANS) code will only resolve the largest scale fluctuations such as periodic vortex shedding. Although such methods will be able to approach the correct mean forces and velocity field, the turbulent fluctuations are unlikely to be correct (Spalart, 2000).

In order to overcome this, large-eddy simulations (LES) can be used. These differ from the RANS methods in that all the turbulent structures are resolved down to the grid scale, while only the turbulence smaller than this scale is modelled. LES should therefore be able to predict the global flow parameters better than a RANS model because all the smaller structures down to grid-scale are resolved.

While RANS models may be able to approximate the mean flow, they cannot fully predict the unsteady flow, due to their inherent averaging which smooths out the smaller eddies. The mean flow given by an unsteady RANS model may not necessarily be the same as an experimentally measured mean. This is why there is an interest in using large eddy simulation (LES) models for this type of separated flow, since it should model most of the turbulent structures down to the grid scale (Rodi, 1997). Not only does this provide a more representative flow field which should correspond to that found experimentally, but it also provides more information regarding unsteady forces which is useful for vibration and noise studies. One of the problems with LES for high Reynolds number flows is that a very large number of cells are required to model the boundary layer down to the wall, however techniques such as using wall functions or RANS/LES hybrid models can be used to overcome this (Spalart, 2000)(Murakami, 1998).

There has not been a great amount of material published on three-dimensional bluff-body simulations. Most of the work has focused on square cylinders and surface-mounted cubes, which have sharp edges which fix the separation point. Rodi (1997) performed a comparison between LES and RANS for the flow around these two geometries. He found that the standard $k-\epsilon$ model overpredicts the turbulence production in the stagnation region. There are modifications to this model which can overcome this. The length of the separation region was overpredicted. LES was able to predict the turbulent fluctuations, and generally predicted the overall flow much better than the RANS.

Murakami (1998) also looked at the surface mounted cube, with broadly similar results. He also found that the standard $k-\epsilon$ model overpredicted the turbulence production but a modified version corrected this. He used a Reynolds stress model (RSM) which gave quite poor results. He concluded that this type of model would need some refinement to work well on this type of flow. The LES results were promising, particularly with the use of a dynamic subgrid-scale model, where the Smagorinsky constant is replaced by a calculated value dependent on the flow field. This overcomes the problem of having to select a value for the Smagorinsky constant which will not be right for the whole flow-field.

One of the main problems with LES for this type of flow is the grid resolution required to resolve the boundary layer correctly, particularly at higher Reynolds numbers. One approach that has been proposed for such situations is a hybrid RANS/LES model. The method developed by Spalart (2000) and Travin (2000) is known as detached eddy simulation (DES). This is based on the Spalart-Allmaras turbulence model (Spalart and Allmaras, 1994) with a simple adjustment to the length scale dependent on the distance to the wall and the cell size. If the cell is close to the wall and is too large for an LES solution the model behaves as the conventional RANS model. Away from the wall, however, the model behaves as a subgrid-scale model and resolves all the energy cascade down to length scales similar to the grid scale.

3 Experimental procedure

3.1 General setup

The experiments were carried out in a wind tunnel with a working section measuring 900mm wide by 600mm high and 2000mm long, with a free-stream turbulence level around 0.3% (Ives et al., 1999 and Cant et al.,2000) . The cylinder had an aspect ratio, $h/d = 1$, with 150mm height and diameter. These dimensions give a Reynolds number based on diameter of 2.9×10^5 at a tunnel speed of 20m/s. The model was made of hollow aluminium tube to allow the fitting of the pressure transducers, and had a removable base which is attached to the dynamometer below the tunnel.

The blockage ratio, defined as the ratio of the frontal area of the model to the cross-sectional area of the tunnel, was 0.07. This would almost certainly lead to an accelerated flow past the cylinder where it is constricted, which means that comparisons with other data should be treated with caution. This is confirmed by Farell et al. (1977) who found that for a blockage ratio of 0.07 the magnitude of the base pressure coefficient, C_{PB}, (the pressure coefficient at the back of the cylinder) would be around 40% greater than with no blockage. However, for the purposes of the current work the computational model is set up to model the effect of the tunnel walls on the flow and so a direct comparison can be made with the experiment. Indeed restricting the domain reduces the uncertainty in the computations.

Various measurements were made of the flow, including surface pressures, using pressure transducers, total forces using a strain-gauge dynamometer, surface flow visualisation, hot-wire anemometry in the wake, and particle image velocimetry to obtain details of the velocity field around the cylinder. Each of these sets of measurements will be described individually below. Conclusions will then be drawn on how these measurements relate to one another to describe the complete flow.

3.2 Ground plate and upstream flow characteristics

One of the problems of mounting a model directly on the floor of the wind tunnel is that of the boundary layer thickness having developed along the length of the contraction. This has been measured at 25mm or $h/6$ at the speed of these tests. In order to reduce the thickness of the boundary layer approaching the model, it was decided to mount the model on a ground plate $55mm$ above the floor of the wind tunnel. This floor was constructed from 5mm board screwed onto blocks to raise it above the tunnel floor. The leading edge was profiled to avoid separation. The model can either be mounted on to a dynamometer or directly to the ground plate. When attached to the dynamometer there is a gap of $\sim 0.5mm$ beneath the model.

It is important to know the nature of the flow upstream of the model so that comparisons can be made between different cases. This information can also be applied to the inlet condition of the CFD model to give a more accurate representation of the flow. The particular features of interest are the turbulence level upstream of the model, the uniformity of the flow across the section and the thickness and nature of the boundary layer on the floor.

Measurements were made using a hot-wire anemometer mounted on the end of a traverse mechanism. The position of the hot wire was measured to an accuracy of $\pm 0.25mm$ with a repeatability of $\pm 0.07mm$. The calibration of the wire was checked frequently during the tests, so that the uncertainty in the velocity is $\pm 1\%$, taking into account the calibration errors and drift during the tests. Profiles of the boundary layer were measured at different locations and speeds to check the uniformity of the flow. Figure 2 shows the profiles at three locations across the tunnel which show that the flow is reasonably symmetrical across the tunnel. These were measured at a streamwise position equivalent to the front of the cylinder. Figure 3 shows the variation in boundary layer thickness with tunnel speed. The nature of the boundary layer can be described by the shape factor, η, where

$$\eta = \delta^* / \theta$$

with δ^* being the displacement thickness and θ being the momentum thickness. For the $U_\infty = 20m/s$ condition $\eta \approx 1.25$, which is close to that found by Klebanoff (1954) for a turbulent boundary layer ($\eta \approx 1.3$), whereas for a laminar boundary layer as described by Blasius (1908) $\eta \approx 2.6$. The slightly smaller shape factor could be due to a favourable pressure gradient in the working section of the tunnel, also Re_θ, at 3000 is lower than the 8000 of Klebanoff. The free stream turbulence level was 0.3%.

3.3 Experimental methods

In order to aid the understanding of the flow topology surface flow visualisation was performed. To do this a mixture of titanium dioxide and paraffin was applied to all the surfaces, which had been covered with black self-adhesive plastic. The tunnel was run for around an hour to allow the paraffin to evaporate leaving the flow pattern visible. It was necessary to leave this to dry overnight to capture the low-speed flow regions.

An important feature of the flow over a body is the pressure distribution generated by the flow on the surface. In an unsteady flow situation however these pressures will be fluctuating with the flow field giving rise to fluctuating forces. A knowledge of the unsteady pressure field is therefore important to the understanding of the flow. The pressure on the surface of the model was measured using a set of five pressure transducers set in the sides of the cylinder. The sensors used were piezoresistive pressure transducers (Endevco Model 8500) with a 2mm diameter silicon diaphragm and a range of 2psi. The five transducers were equally spaced along a generator of the cylinder ($z/d = 0.17$ to 0.83) and then the cylinder was rotated on the dynamometer base through 360 degrees at 5 degree intervals so that a full picture of the surface pressures could be gathered.

Although calibration data for the transducers had been provided by the manufacturer, when the first measurements were made the results were clearly incorrect. Further investigation revealed that the sensitivity was affected quite significantly by the mounting method. It is imperative not to apply any load to the barrel of the transducer as this will distort the diaphragm. The manufacturer's advice was sought and they recommended the use a flexible adhesive such as RTV. Tests with this show that the sensitivity is closer to that stated by the manufacturer but it is still significantly different. The transducers therefore had to be calibrated in position in the model. This was achieved by attaching pressure tubes to the transducer holes and measuring the mean pressure using a micromanometer.

The forces acting on the model were to be measured using a dynamometer mounted underneath the tunnel. A single component strain gauge dynamometer was used which had a sensitivity of $74\mu V/N$. The dynamometer was rotated to measure either lift or drag. The dy-

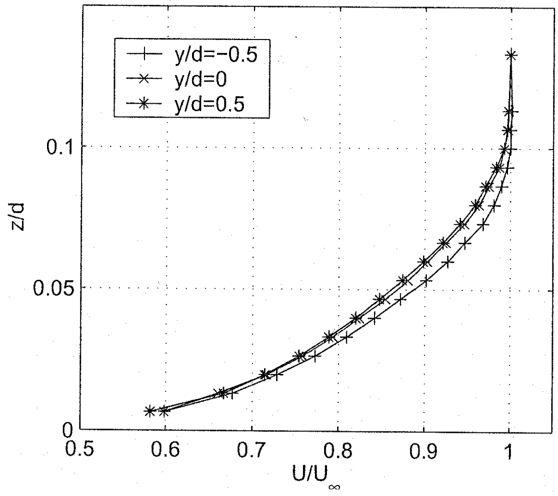

Figure 2: Plot of the normalised U velocity in the boundary layer across the tunnel ($x/d = -0.5$) at $U_\infty = 20m/s$

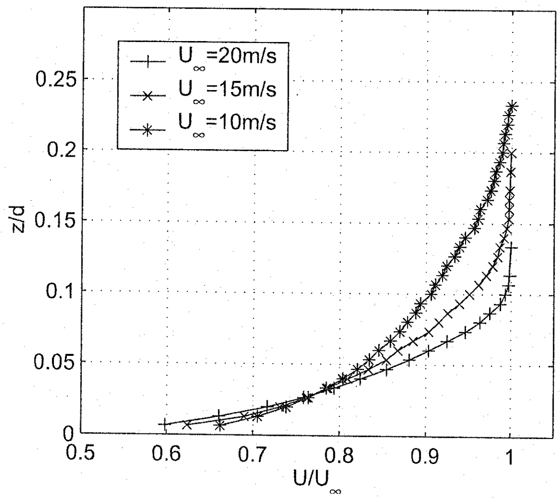

Figure 3: Plot of the normalised U velocity in the boundary layer at various speeds ($x/d = -0.5$)

namometer was connected to a Fylde bridge balance and power supply. The amplified signal was then processed by an analogue to digital converter and software such as LabView was used to record the values. Calibration was achieved by attaching weights suspended over a pulley. This process was repeated for every set of measurements. A series of four weights were used up to $2.41kg$.

For the PIV measurements the laser was mounted on top of the wind tunnel with a narrow slot in the roof for the light to pass through. The laser could be rotated to give a light sheet in either the longitudinal, xz, plane or the transverse, yz, plane. The camera was positioned either beside the tunnel pointing through a side window, or inside the tunnel, downstream of the model. The image size in the longitudinal plane was $292 \times 233mm$ and in the transverse direction $225 \times 180mm$. In the transverse plane this was sufficient to cover the entire wake region near the model. In the longitudinal direction it was necessary to take three images from the front of the cylinder to two diameters downstream. Seeding was provided by a smoke generator outside the tunnel exit. The smoke thus had time to diffuse before entering the tunnel.

Tests were carried out to determine the optimum timing between laser flashes, as it is important that the particles do not travel too far in between flashes. It was found that an interval of $15\mu s$ gave good results. In order to get a large set of data to calculate the mean flow and other statistical values, 1000 images were taken in each position. The cross-correlation was performed using 32×32 pixel squares with a 50% overlap. A range validation was used to eliminate anomalous points based on the magnitude of velocity, and a moving average filter was applied to interpolate for the missing points.

3.4 Errors and uncertainties

The errors in the pressure measurements were estimated using the method of Moffat (1988). The fixed errors were estimated as follows: $\pm 0.20mmH_2O$ for the transducers, based on the manufacturers data and $\pm 0.05mmH_2O$ for the two micromanometers. Other sources of error such as the analogue to digital converter were considered to be negligible. This leads to a fixed calibration error of $\pm 0.21mmH_2O$, and a total measurement error of $\pm 0.30mmH_2O$ or $\sim \pm 1.2\%$ at $25mmH_2O$. The frequency response is flat up to 20% of the resonant frequency, $70000Hz$, which covers the range of interest. The variable errors, i.e. the non-repeatability of the measurements has been estimated from a series of 30 readings at the same condition. This gives a standard deviation, σ, of $0.017mmH_2O$ at a mean pressure of $-3.483mmH_2O$. This corresponds to a variable error, $2\sigma = \pm 1\%$ of the mean. 95% of the samples will lie within this band. The total uncertainty is therefore ±1.4%.

The variable error in the force measurements is estimated by taking a series of 30 readings with a fixed load applied to the dynamometer. This gives a standard deviation of $0.0034N$ at a load of $0.73N$, or $\pm 0.5\%$. The fixed error is $\pm 0.01N$. The total uncertainty in the force measurements is $\pm 0.5\%$.

4 Experimental results and discussion

4.1 Flow visualisation

The photographs in Figure 4 show the results of this visualisation, at $U_\infty = 20m/s$, with the flow from left to right. The side view of the cylinder, shows that the flow is attached up to 70 deg from the leading edge. This angle has been measured directly to an accuracy of ± 0.5 deg. The separation line is bent backwards towards the tip as the upwash delays separation. The view from the front also shows the attached flow behind the stagnation point. On the top there is a region of reversed flow. This flow then wraps into a pair of vortices one-third of the distance from the leading edge. This also draws fluid up from the sides behind the separation line. On the floor the line of the horseshoe vortex is clearly visible.

4.2 Measurement of surface pressures

Figure 5 shows the mean surface pressure coefficient, C_p around the circumference of the cylinder at different heights above the floor, at $U_\infty = 20m/s$. The plot shows that the pressure coefficient starts at 1 at the stagnation point on the leading edge and then falls rapidly to a minimum point, $C_p \approx -1.4$ at around 65 deg, before rising slightly and levelling out in the wake region. The base pressure coefficient is around 1, though it is varying with height. At the stagnation point the highest C_p is at the mid-height position with the pressure dropping very slightly towards the base and more towards the tip. The minimum pressure is lowest at the top of the cylinder as well. The minimum pressure coefficient is slightly lower than the -0.8 found by Okamoto (1982), but his tests were at a lower Reynolds number, 4.74×10^4.

The plots of power spectral density function in Figure 6 show that there are no strong peaks in the energy spectrum of the pressure signals, apart from a small one at $12Hz$. This indicates that there is no periodic vortex shedding in the wake of the cylinder. This is in agreement with Luo et al (1996) and Kawamura et al (1984) who found that there was no such shedding on low-aspect ratio cylinders.

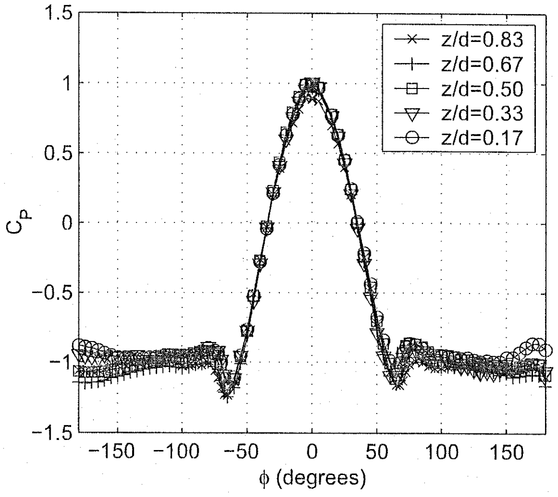

Figure 5: Distribution of pressure coefficient around cylinder, $U_\infty = 20m/s$

4.3 Dynamic force measurements

The mean drag coefficients were found at a range of speeds and are plotted in Figure 7. Here the drag coefficient uses the standard definition using the freestream velocity, U_∞ and the frontal area of the cylinder. Plots of the power spectral density function of the signals are shown in Figure 8. The strong peaks at around $11Hz$ and $16Hz$ in the drag, and at $13Hz$ and $21Hz$ in the lift appear to be natural frequencies of the system. The more interesting characteristics are the next broadband peaks at $24Hz$, $36Hz$ and $48Hz$ at $10m/s$, $15m/s$ and $20m/s$ respectively. These correspond to a Strouhal number, $Str = \frac{fd}{U_\infty}$, of 0.36. Due to the absence of any such peaks in the pressure measurements, it is unclear at present where this force fluctuation originates.

4.4 PIV measurements

Figure 9 gives the mean longitudinal velocity contours while Figure 10 compares the mean vorticity with the velocity vectors. Figure 11 compares the instantaneous velocity field with the mean flow. The longitudinal streamlines show that the flow separates at the top edge of the cylinder and is reversed over most of the length, before forming a large recirculation region behind the body around 1 diameter in length. The transverse cuts clearly show the formation of a pair of counter-rotating vortices at the top of the cylinder along with the weaker horseshoe vortex at the base. The counter-rotating vortices move downwards in the downstream direction with the descending shear layer, and also expand, so that 2 di-

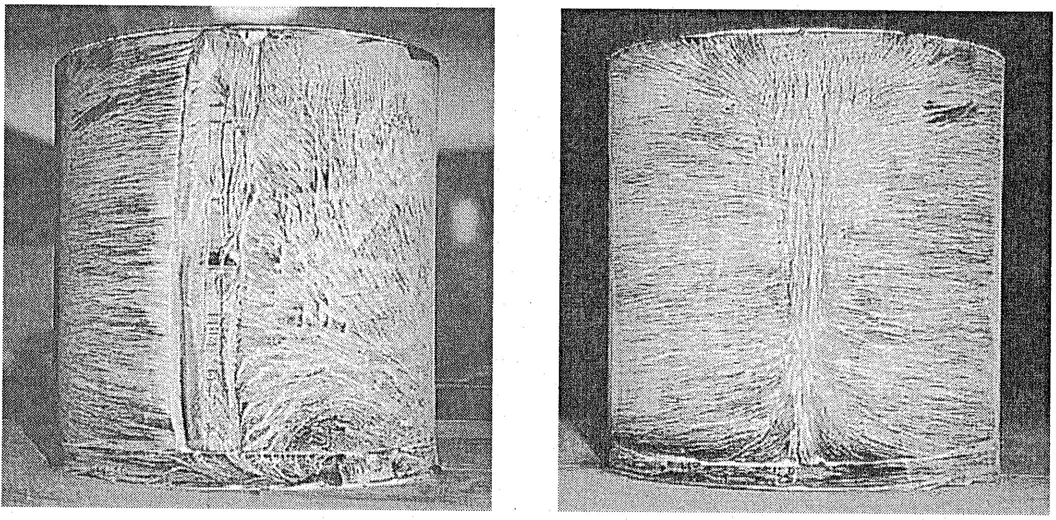

(a) Side of cylinder (flow left to right)

(b) Front of cylinder (flow into page)

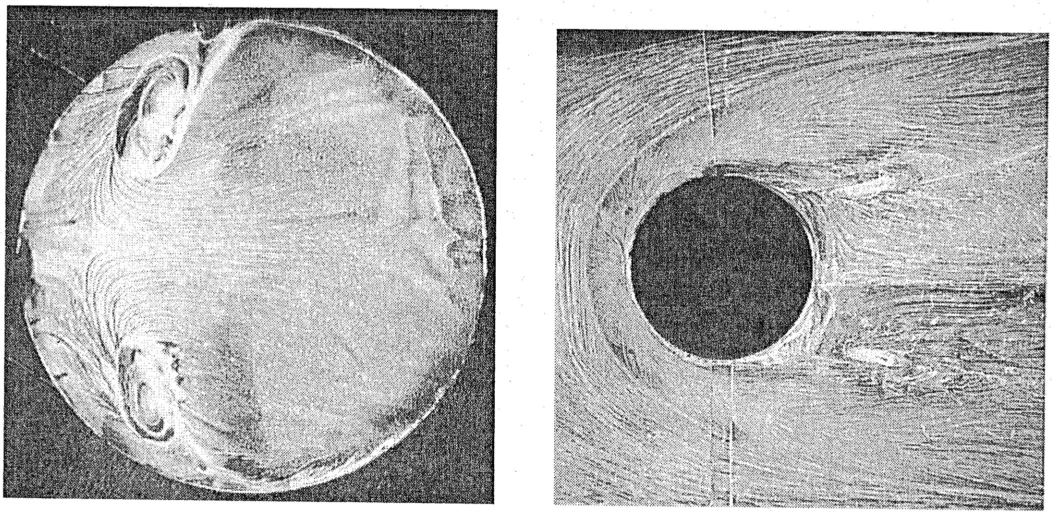

(c) Top of cylinder (flow left to right)

(d) Floor of tunnel (flow left to right)

Figure 4: Surface flow visualisation pictures

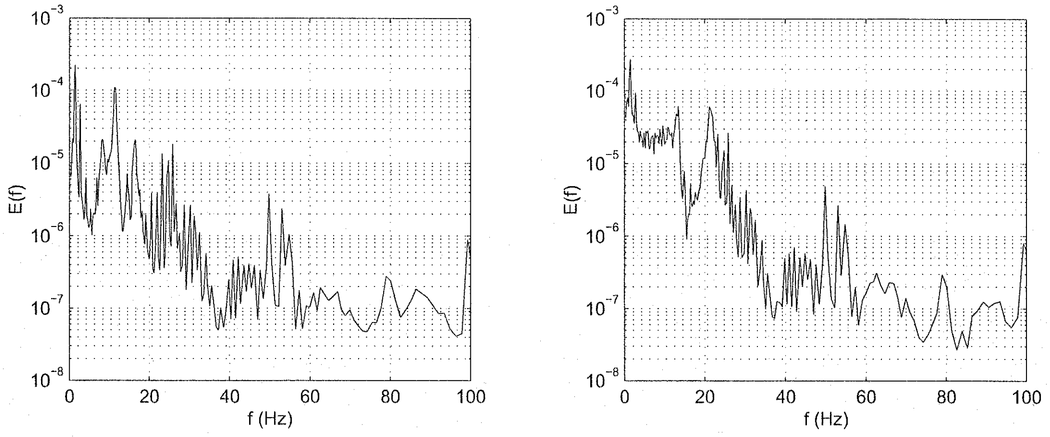

(a) Drag, $U_\infty = 10m/s$

(b) Lift, $U_\infty = 10m/s$

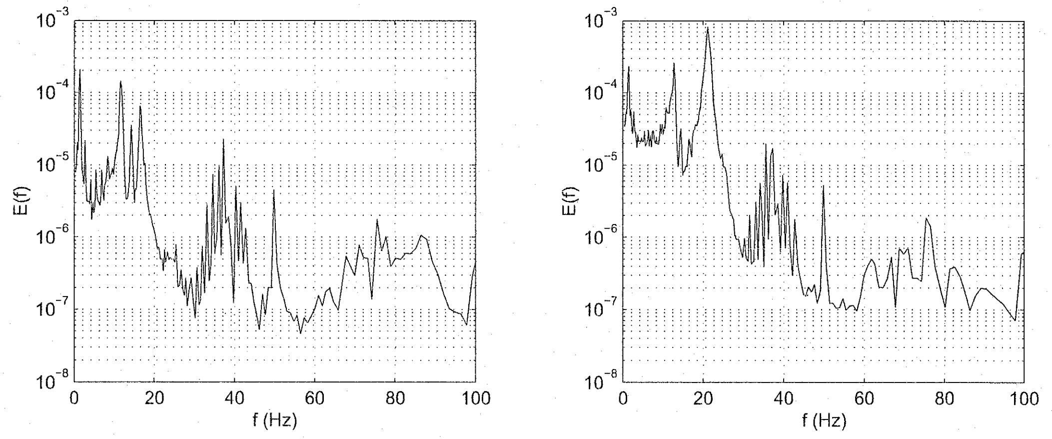

(c) Drag, $U_\infty = 15m/s$

(d) Lift, $U_\infty = 15m/s$

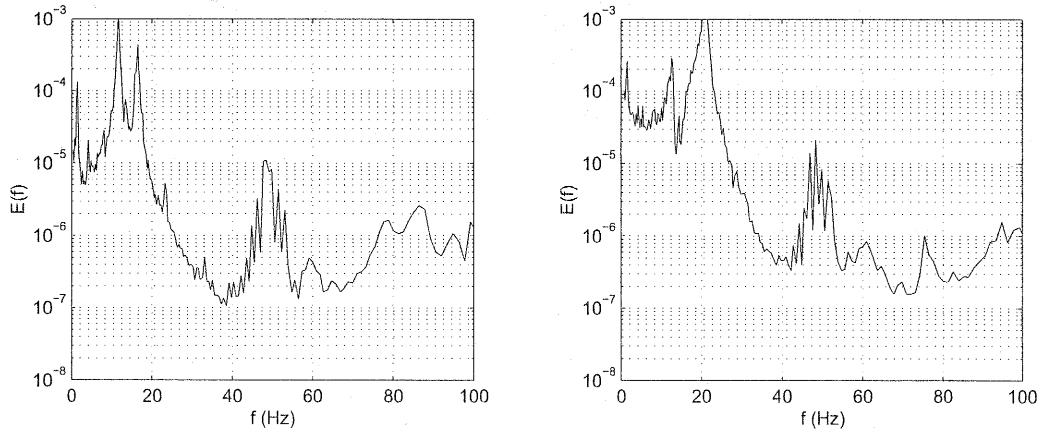

(e) Drag, $U_\infty = 20m/s$

(f) Lift, $U_\infty = 20m/s$

Figure 8: Power spectral density function of force signals

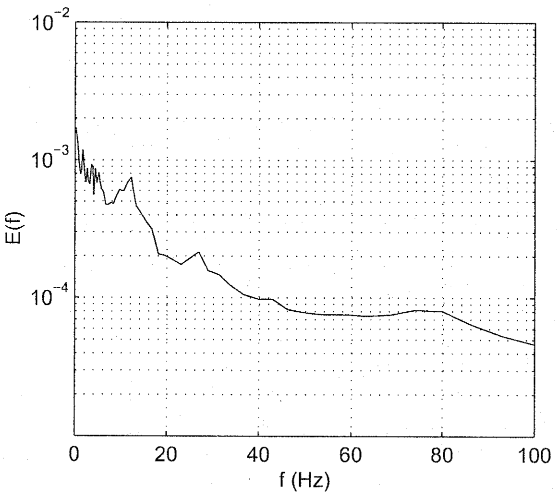

(a) 135 degrees

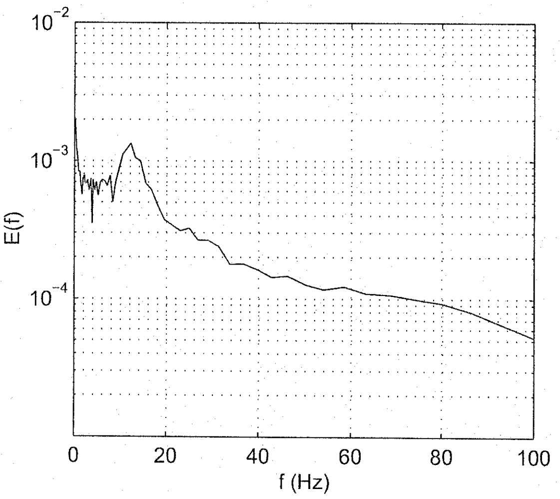

(b) 180 degrees

Figure 6: Power spectral density function of pressure measurements at $z/h = 0.5$

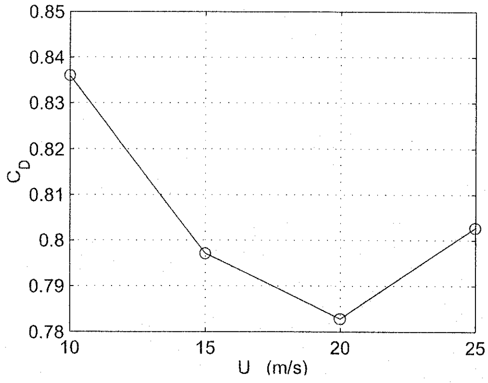

Figure 7: Mean drag coefficients

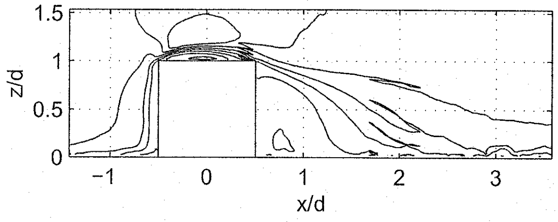

Figure 9: U velocity contours $y/d = 0$, measured by PIV

ameters downstream they are quite large and in contact with the ground. In the instantaneous images the flow picture is much more chaotic as the counter-rotating vortices move around and other vortices appear in the wake region. Similarly in the longitudinal plane the shear layer could be seen to move substantially with turbulent vortices being formed underneath it. The turbulence intensities were very large around the shear layer due to movement of this layer. It is not possible to identify any periodicity from these images as the maximum frequency of the laser was only 8Hz and so hot-wire measurements would be needed to determine any dominant frequencies.

5 Computational results

The computational simulations were carried out using a code developed at the University of Southampton (Bresslof, 2001) which is a fully parallel finite volume solver with a range of turbulence models and numerical schemes available. Two different methods were investigated, RANS solutions with a $k - \epsilon$ turbulence model, and an LES simulation using the structure function model. Second order differencing was used throughout, and the SIMPLEC pressure-correction method was em-

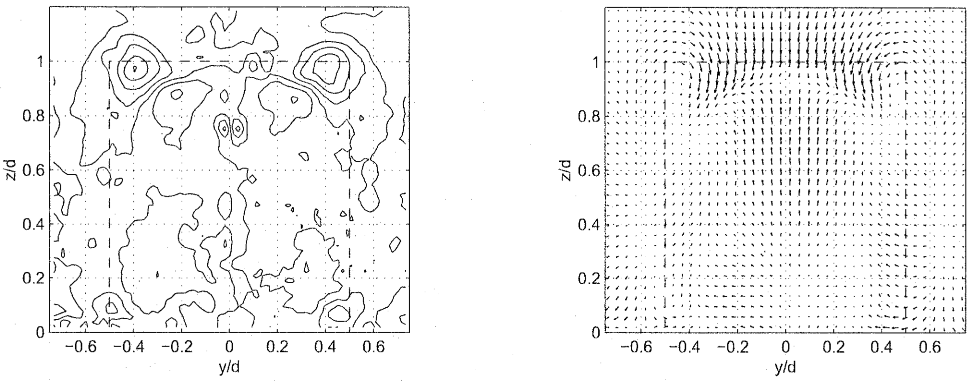

(a) Vorticity contours $x/d = 0.17$

(b) Velocity vectors $x/d = 0.17$

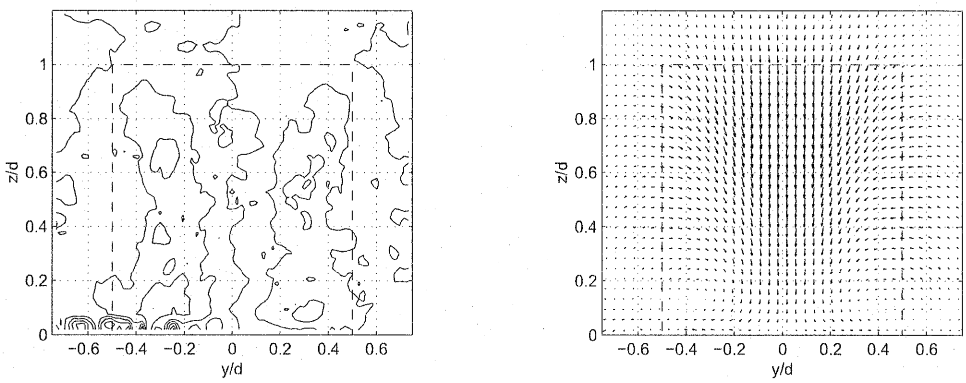

(c) Vorticity contours $x/d = 1.0$

(d) Velocity vectors $x/d = 1.0$

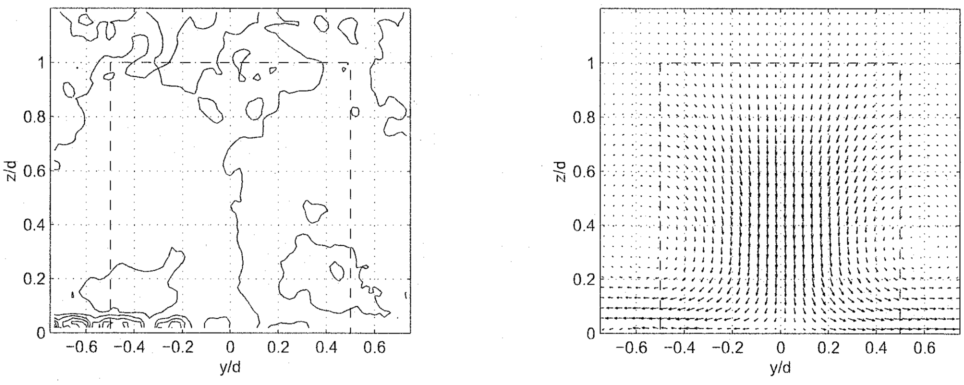

(e) Vorticity contours $x/d = 2.0$

(f) Velocity vectors $x/d = 2.0$

Figure 10: PIV measurements of vorticity and velocity

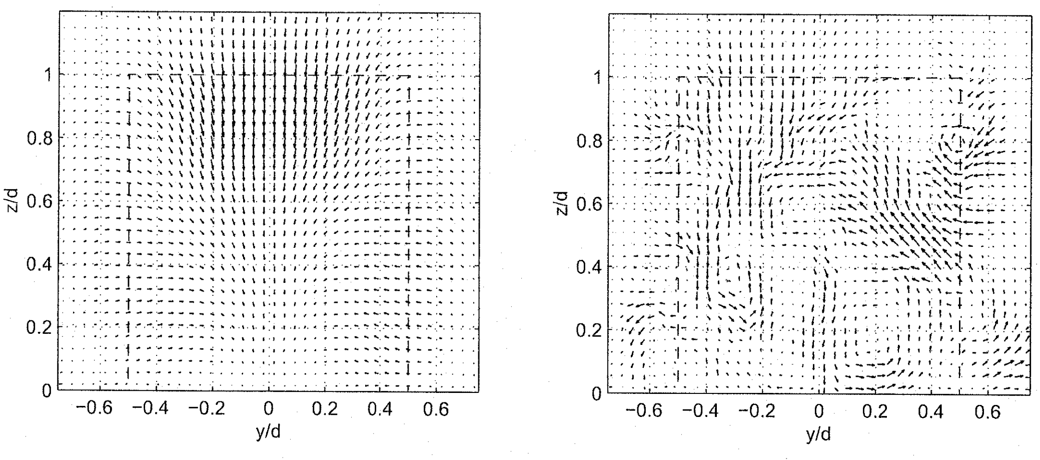

(a) Mean

(b) Instantaneous

Figure 11: PIV measurements of velocity at $x/d = 0.5$

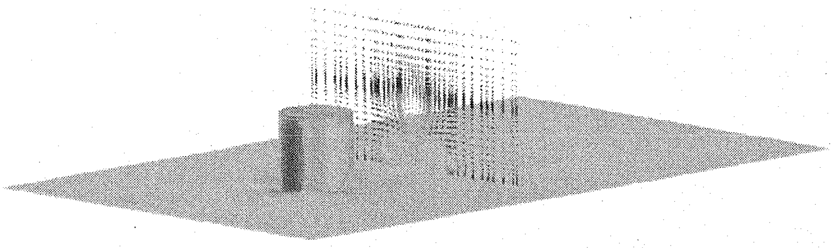

Figure 12: Numerical solution from CFX4.3 showing surface pressure contours and vector field behind cylinder

ployed. The solver uses the MPI libraries to allow parallel computation on a cluster of PCs. All the computations were carried out on 16 nodes each with 2 1GHz processors and 512Mb of RAM.

The LES simulations were carried out using the structure-function model as proposed by Métais and Lesieur (1992). Here the eddy viscosity is given by,

$$\nu_t = 0.105 C_K^{-3/2} \Delta x F_2^{1/2}$$

where,

$$F_2 = \langle \|\overline{u}(\mathbf{x},t) - \overline{u}(\mathbf{x}+\mathbf{r},t)\|^2 \rangle_{\|\mathbf{r}\|=\Delta x}$$

C_K is the Kolmogorov constant and Δx is the cell size.

The grids were constructed using Fleximesh (Rycroft, 1997), and designed to match the geometry of the model in the wind tunnel working section, including the walls. They were composed of 32 structured blocks, arranged as shown in Figure 13. The cells were clustered towards the walls of the cylinder and the floor of the tunnel as shown in Figure 14. The cell size on the floor of the tunnel was $0.0021d$ and on the cylinder walls $0.0006d$. The domain size was $3.0h$ upstream of the cylinder, $6.7h$ downstream, $6.0h$ laterally and $4.0h$ vertically. No-slip conditions were applied to the walls of the tunnel, although the grid was not fine enough here to resolve the wall flow. A uniform velocity was applied to the inlet and a zero-gradient condition to the outlet. The $k - \epsilon$ model was applied to three grids of increasing numbers of cells as detailed in Table 1. The numbers of cells in each direction were multiplied by two each time, keeping the first cell size constant. The LES simulation was carried out on the medium density grid.

Table 1 also shows the positions of separation on the cylinder side and on the ground plane upstream, as well as

Run No	Model	Cells	CPU	Separation (degrees)	Fwd sep (x/d)	Reattachment (x/d)	Local Cd (z/d=0.5)
1	$k-\epsilon$	1,015,360	61 hrs	106.6	-0.78	2.07	0.51
2	$k-\epsilon$	2,052,480	120 hrs	107.2	-0.79	2.14	0.50
3	$k-\epsilon$	4,020,000	249 hrs	105.9	-0.79	2.11	0.39
4	LES	2,052,480	87 hrs	82.8	-1.48	1.55	0.81
Experimental				70		1.56	1.14

Table 1: Details of grids and results

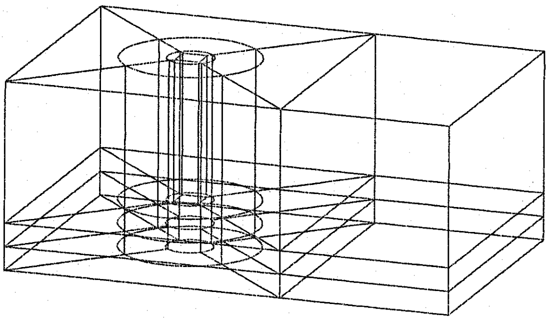

Figure 13: Diagram showing arrangement of blocks in the computational grid

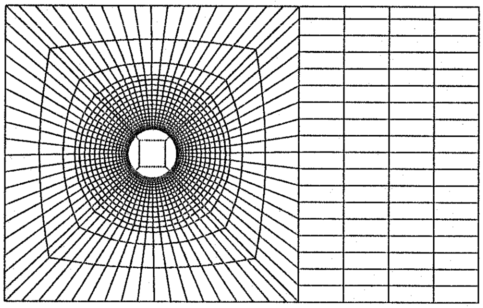

Figure 14: Representation of the computational grid (not all cells drawn)

the reattachment point on the ground downstream and the local drag coefficient at the mid-height. Looking first at the three $k-\epsilon$ cases, it can be seen that there is little difference between the three grids in terms of separation and reattachment, although all are significantly different to the experimental values. The prediction of separation from the cylinder side is particularly poor. The reattachment length is 34% greater than the experimental value, which is in agreement with the findings of Rodi (1997) for the surface mounted cube case. The LES solution in contrast gives much closer agreement in the separation from the side and in the reattachment position, which is very close. However, the forward separation point, and the form of the horseshoe vortex is not captured correctly. This may be a limitation due to not resolving the wall region sufficiently on the ground plane. A wall function may be necessary to overcome this.

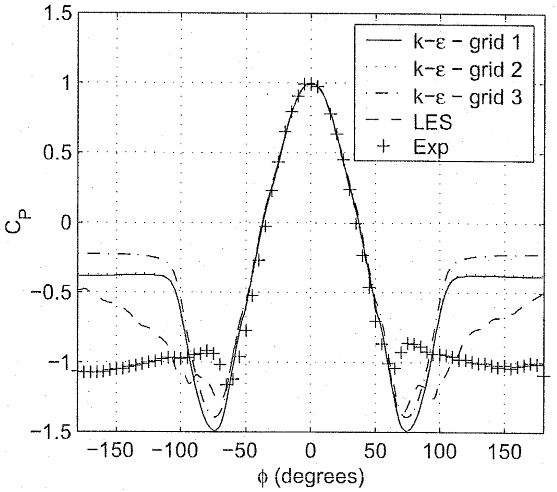

Figure 15: Plot of Cp around cylinder at $z/d = 0.5$ for different grids

The predicted local drag coefficients are widely scattered. The curves in Figure 15, which show the pressure distribution at $z = 0.5$ for the different cases, indicate that the pressure on the forward part of the cylinder is well predicted by all, but the base pressure at the rear is not. The LES simulation is again better than the $k-\epsilon$, but this could be linked to the late separation in the case of the $k-\epsilon$ models is also a factor. Figure 16 shows the pressure coefficient around the cylinder at five heights for the $k-\epsilon$ case, corresponding to those in Figure 5. The main difference is that the separation point is much further back than in the experimental case, causing the minimum pressure to be further back and also of greater magnitude.

Figure 17 presents a plot of U-velocity along the cen-

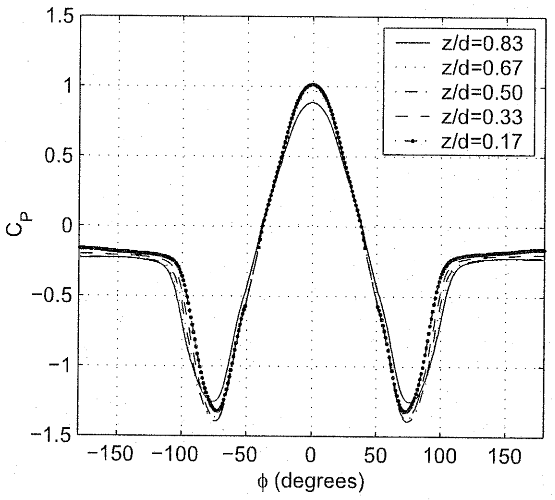

Figure 16: Plot of Cp around cylinder using $k-\epsilon$ model (Grid 3)

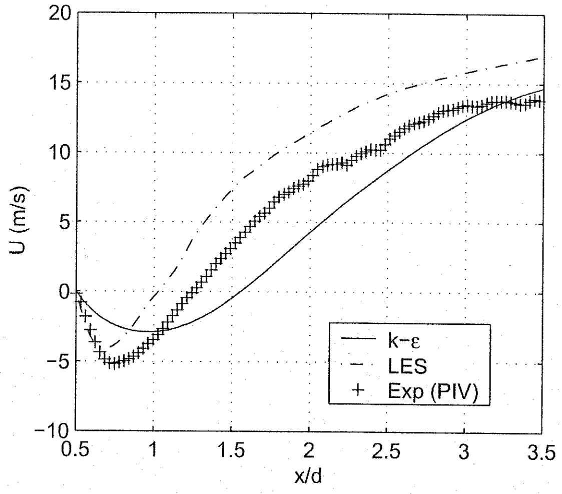

Figure 17: Plot of U velocity at $y=0$, $z=0.5$

treline of the tunnel at a height of $z/d=0.25$ downstream of the cylinder. This highlights the difference in the length of the recirculation region between the $k-\epsilon$ models and the LES and experimental results. The LES curve is much closer to the experimental data.

6 Conclusion

This series of experiments has provided a large amount of data on the flow over a low aspect ratio cylinder. The main features of the flow have been identified as being the counter-rotating vortices off the top edges of the cylinder, the horseshoe vortex at the base and a turbulent recirculation region behind the cylinder. The flow separates from the cylinder at 70 degrees as can be seen from both the flow visualisation and the pressure measurements. In the wake region the trailing vortices from the tip merge with the horseshoe vortex at the base, eliminating any von Karman vortex shedding. The recirculation region is a region of highly turbulent flow. There is a broad band frequency signal in the force measurements corresponding to a Strouhal number of 0.36. This set of data is a good basis for validating CFD codes as it is comprehensive with constant known conditions for all measurements. The PIV measurements in particular will enable a comparison of full planes of data rather than single values.

Limited numerical simulations have been carried out using two different numerical models, RANS and LES. These simulations confirm that this is a difficult case to model accurately and so further work must be carried out to improve on the results. The RANS model gave rather poor results, particularly in the prediction of the separation point and the flow on top of the cylinder. The LES simulations gave better results with an earlier separation point and more accurate recirculation length. Further work is on-going to allow the use of DES to capture results on grids on reasonable size.

References

Ayoub, A. and Karemcheti, K., "An experiment on the flow past a finite circular cylinder at high subcritical and supercritical reynolds numbers," Journal of Fluid Mechanics, vol. 118, 1982, pp. 1–26.

Baker, C., "The laminar horseshoe vortex," Journal of Fluid Mechanics, vol. 95, no. 2, 1979, pp. 347–367.

Bressloff, N., "A parallel pressure implicit splitting of operators algorithm applied to flow at all speeds," Int Jnl of Numerical Methods in Fluids, vol. 36, 2001, pp. 497–518.

Cant, C., Lait, E., Hankins, N., and Mason, R., "The design, build and commissioning of an aerodynamic test facility," MEng Group Design Project Report, University of Southampton, School of Engineering Sciences, Ship Science, 2000.

Farell, C., Carrasquel, S., Guven, O., and Patel, V., "Effect of wind tunnel walls on the flow past circular cylinders and cooling tower models," Trans ASME Journal of Fluids Engineering, vol. 99, 1977, pp. 470–479.

Farivar, D., "Turbulent uniform flow around cylinders of finite length," AIAA Journal, vol. 19, 1981, pp. 275–281.

Ives, N., Scott, D., Silva, F. d. A., and Walker, M., "Design and construction of an aerodynamic test facility," MEng Group Design Project Report, University of Southampton, Ship Science, 1999.

Kawamura, T., Hiwada, M., Hibino, T., Mabuchi, I., and Kumuda, M., "Cylinder height greater than turbulent boundary layer thickness - flow around a finite circular cylinder on a flat plate," Bulletin of the JSME, vol. 27, no. 232, 1984, pp. 2142–2151.

Klebanoff, P., "Characteristics of turbulence in a boundary layer with zero pressure gradient," TN 3178, NACA, 1954.

Luo, S., Gan, T., and Chew, Y., "Uniform flow past one (or two in tandem) finite length circular cylinders," Journal of Wind Engineering and Industrial Aerodynamics, vol. 59, no. 1, Jan 1996, pp. 69–93.

Métais, O. and Lesieur, M., "Spectral large-eddy simulations of isotropic and stably-stratified turbulence," Journal of Fluid Mechanics, vol. 239, 1992, pp. 157–94.

Moffat, R., "Describing the uncertainties in experimental results," Experimental Thermal and Fluid Science, vol. 1, 1988, pp. 3–17.

Murakami, S., "Overview of turbulence models applied in CWE-1997," Journal of Wind Engineering and Industrial Aerodynamics, vol. 74-76, 1998, pp. 1–24.

Okamoto, S., "Turbulent shear flow behind hemisphere-cylinder placed on a ground plane," in "Turbulent Shear Flows," vol. 3, Springer-Verlag, 1982, pp. 171–185.

Okamoto, S. and Sunabashiri, Y., "Vortex shedding from a circular cylinder of finite length placed on a ground plane," Trans ASME Journal of Fluids Engineering, vol. 114, Dec 1992, pp. 512–521.

Okamoto, T. and Yagita, M., "The experimental investigation on the flow past a circular cylinder of finite length," Bulletin of Japan Soc Mech Eng, vol. 16, 1973, pp. 805–814.

Park, C.-W. and Lee, S.-J., "Free end effects on the near wake flow structure behind a finite circular cylinder," Journal of Wind Engineering and Industrial Aerodynamics, vol. 88, 2000, pp. 231–246.

Rodi, W., "Comparison of LES and RANS calculations of the flow around bluff bodies," Journal of Wind Engineering, vol. 69-71, 1997, pp. 55–75.

Rycroft, N., "Three-dimensional multi-block grid generation - fleximesh," Ship Science Report 101, University of Southampton, November 1997.

Sin, V. and So, R., "Local force measurements on finite span cylinders in a cross-flow," Trans ASME Journal of Fluids Engineering, vol. 109, no. 2, June 1987, pp. 136–143.

Spalart, P., "Strategies for turbulence modelling and simulations," International Journal of Heat and Fluid Flow, vol. 21, 2000, pp. 252–263.

Spalart, P. and Allmaras, S., "A one-equation turbulence model for aerodynamic flows," La Recherche Aerospatiale, , no. 1, 1994, pp. 5–21.

Sumer, B., Christiansen, N., and Fredsœ, J., "The horseshoe vortex and vortex shedding around a vertical wall-mounted cylinder exposed to waves," Journal of Fluid Mechanics, vol. 332, 1997, pp. 41–70.

Travin, A., Shur, M., Strelets, M., and Spalart, P., "Detached-eddy simulations past a circular cylinder," Flow Turbulence and Combustion, vol. 63, 2000, pp. 293–313.

Visbal, M., "Structure of laminar juncture flows," AIAA Journal, vol. 29, no. 8, 1991, pp. 1273–1282.